Analytical modeling of the steady state ablation of a 3D C/C composite

Jean Lachaud, Yvan Aspa, Gerard L. Vignoles

Analytical modeling of the steady state ablation of a 3D C/C composite

J. Lachaud [a,*] , Y. Aspa [a,b] , and G. L. Vignoles [a]

[a]Université Bordeaux 1
Laboratoire des Composites ThermoStructuraux (LCTS)
3, Allée de La Boétie, 33600 Pessac, France

[b]Institut de Mécanique des Fluides de Toulouse (IMFT)
1, allée Prof. Camille Soula, 31000 Toulouse, France

Abstract

Following an analysis of surface roughness features that develop on a 3D C/C composite during ablation, *i.e.* wall recession by oxidation and/or sublimation, a modeling strategy is set up in order to predict the composite behavior from that of its components. It relies on two changes of scale: (i) microscopic scale (fiber, matrix) to mesoscopic scale (bundle) and (ii) mesoscopic scale (bundle, matrix) to macroscopic scale (composite). The physical basis is a general model for receding surfaces under a gasification process coupled to mass transfer. At each scale, the 3D surface equation is analytically solved in steady state considering a 1D mass transfer perpendicular to the overall surface. The models are validated by comparison to experimental data.

Key words: Carbon-carbon composites, ablation, moving interface, changes of scale, phenomenological model

1 Introduction

Carbon/Carbon (C/C) composites, which keep excellent mechanical properties at high temperatures [1], are used as thermostructural protections in various applications such as atmospheric re-entry (vehicle thermal protection systems) [2, 3], propulsion (rocket nozzle) [4, 5], and experimental Tokamak reactors for nuclear fusion (divertor and first wall armor) [6, 7]. In these applications, the C/C composites are progressively destroyed by oxidation (re-entry and propulsion), sublimation (re-entry and Tokamaks), and, up to a certain extent, plasma etching (Tokamaks), and thermo-mechanical erosion (all cases). These degradation processes, resulting in a high interfacial mass transfer, induce a non negligible recession of the wall called ablation.

* Tel.: +33 663 863 913; *fax:* +33 556 841 225. *E-mail address:* jean.lachaud@gadz.org

Nomenclature

A	ablation rate contrast	*Greek symbols*	
C	molar concentration, $mol \cdot m^{-3}$	α	angle of fiber tip, rad.
D	diffusion coefficient, $m^2 \cdot s^{-1}$	γ	angle of a surface orientation, rad.
Da	Damköhler number	δ	boundary layer thickness, m
F, f	functions	Ω	molar volume, $m^3 \cdot mol^{-1}$
h	roughness features height, m	*Subscripts and superscripts*	
J	molar flux, $mol \cdot m^{-2} \cdot s^{-1}$	$\bullet_b$	relative to bundles
k	reactivity, $m \cdot s^{-1}$	$\bullet_c$	relative to concentration
l	yarn section, m	$\bullet_C$	relative to the composite
$\mathcal{L}$	ablation characteristic length, m	$\bullet_e$	relative to any composite element
Kn	Knudsen number	$\bullet^{eff}$	effective value
r, θ, z	cylindrical space coordinates, m	$\bullet_f$	relative to fibers
R	radius, m	$\bullet_g$	relative to gas
S	function describing the surface	$\bullet_i$	relative to intra-bundle interphase
Sh	Sherwood number	$\bullet_{i-b}$	relative to inter-bundle interphase
t	time, s	$\bullet_m$	relative to bulk matrix
v	velocity, $m \cdot s^{-1}$	$\bullet_s$	relative to a solid phase
x, y, z	cartesian space coordinates, m	$\widetilde{\bullet}, \widehat{\bullet}$	dimensionless values

An efficient design of a thermostructural protection relies on an accurate evaluation of its ablation behavior. While fluid and plasma dynamics are now correctly modeled and simulated [4, 7, 8], the complex behavior of C/C composites is not fully understood [9], and consequently not taken accurately into account in the models [10]. Due to the progress of the computational hardware and software, which enables to handle richer models, the demand of an accurate description and modeling of the material behavior has increased, especially as far as surface roughness is concerned [2, 10]. Indeed, ablation of C/C composites is known to lead, among others, to a typical surface roughness. The surface roughening, which is inseparable from global recession, influences strongly other phenomena. First, it increases the active surface of the wall; this induces an enhancement of heat and mass transfer at the interface [11]. Second, the onset of the surface roughness leads to a complex composite behavior: the effective ablation velocity of the composite can not be modeled using a simple arithmetic average of the ablation velocities of its components [9,12]. Third, for re-entry and propulsion, it can trigger mechanical erosion, since a high speed flow surrounds the protection. Fourth, in the case of high velocity re-entries, it contributes to the laminar-to-turbulent transition in the dynamic boundary layer. PANT (Passive Nosetip Technology) program results show that the heat flux may be multiplied by a factor of up to three in turbulent regime [13].

Therefore, the understanding of the interaction between the material and its close environment has to be improved for all of these applications. To date, the lack of knowledge is balanced by many data from plasma-jet experiments, which provide the composite behavior in the tested conditions. Experimental

results are then used as input data for the global scale simulations [2, 8, 10]. Using this method, extrapolation is of poor reliability. To improve the extrapolation, some phenomenological interpretations of the onset of surface roughness caused by a thermo-mechanical ablation have recently been proposed [6, 14]. In a complementary way, this work focuses on physico-chemical ablation by oxidation.

This paper is organized as follows. In the first section, the experimental behavior of a C/C composite is analyzed. The typical surface roughness that develops on the material architecture during ablation is observed, analyzed and classified. In the second section, a multiscale modeling strategy based on these analyses is proposed; it includes two changes of scale. In the third section, the mesoscopic scale properties are assessed from the microscopic ones (first change of scale). In the fourth section, the macroscopic scale properties are inferred from the mesoscopic ones (second change of scale). In the last section, the multi-scale model is validated by comparison to experimental data presented in [9].

2 Experimental analysis

2.1 Ablation test

A C/C composite sample has been ablated in a cylindrical oxidation reactor at a controlled temperature ($625°C$) under dry air at atmospheric pressure. The average velocity of the flow is $1\, m \cdot s^{-1}$. This value is chosen to ensure a high laminar oxygen injection flow in order to avoid reaction limitation by diffusion. Simultaneously, the mass Péclet number close to the sample surface has been shown to be low, *i.e.* the advection velocity close to the sample is negligible when compared to the mass diffusion velocity. Moreover, mass transfer has been shown to be perpendicular to the sample surface. A complete description of the reactor and the CFD modeling of the experiment are provided in [9].

2.2 Material analysis

The studied material is a 3D C/C composite, made from a 3D ex-PAN (PolyAcryloNitrile) carbon fiber preform and a pitch-based carbon matrix. It is a heterogeneous multi-scale material. Several thousands of fibers are linked together into a unidirectional bundle with a pitch-based matrix. Then, bundles are orthogonally fit together into a pattern repeated by translation on a cubic lattice. This macrostructure leads to a network of parallelepipedic macropores (located near each node of the lattice), which are partially filled with pitch matrix and are called *octets*. The composite has then been graphitized [9].

The surface of the ablated sample has been analyzed by scanning electron microscopy (SEM). 3D C/C composite oxidation leads to the onset of a steady state, multi-scale surface roughness. Also, the surface roughness morphologies observed in this study are similar to the morphologies obtained with traditional plasma-jet tests [15–17]. The SEM micrographs of figure 1 illustrate the material ablative behavior :

- A macroscopic surface roughness takes place on the lattice of the composite (micrograph M). It seems to result from the difference of reactivity between bundles and a weak interphase that surrounds them. This inter-bundle interphase is deeply ablated and perpendicular bundles feature a pyramidal shape. Parallel bundles and matrix octet surface are slightly undulating and are slightly lower than perpendicular bundle tips.

- A mesoscopic surface roughness develops at the end of emerging bundles, and looks like *needle clusters* (micrograph a_μ) -resp. *needle layers* (micrograph c_μ)- for bundles perpendicular -resp. parallel- to material surface. In the literature, many micrographs display such roughness features on carbon-based composites during ablation by oxidation [18–20] or both oxidation and sublimation [15, 21, 22]. A thin interphase lying between fibers and bulk matrix is very reactive. The recession velocity of the interphase is then higher than for fibers and bulk matrix. Therefore, fibers and bulk matrix are partially stripped, become thinner, and acquire a needle shape.

- A microscopic surface roughness appears on the fibers and on the matrix octets. Fiber tips are faceted (micrograph a_μ and c_μ). The matrix octets show denuded layers arranged in a parallel fashion (micrograph b_μ). This is consistent with their pseudo-crystalline anisotropic structure [17, 19].

From the above presented descriptions and classifications, it appears that ablation-related geometrical features of the rough surface mainly follow the material structure. Accordingly, it will be called structural roughness to make a difference with a purely physical roughness, which has already been observed on homogeneous materials and modeled [3]. This physical roughness consists in scalloped morphologies and is not correlated to material structure. It relies on the competition between bulk and heterogeneous mass or heat transfers. These phenomena may also be of importance in the present case. As a result, models including structure and physics have to be taken in consideration.

3 Multi-scale modeling strategy

The modeling strategy focuses on the material behavior, *i.e.* on the differential recession of its heterogeneous surface that leads to the onset of surface roughness. The macroscopic motion of an interface between two media caused by the action of heterogeneous transfer can be interpreted as an advancing wavefront with a normal velocity equal to that of the interface. The interface is synonymously referred to as the surface function S. The interface position is commonly described in cartesian coordinates by the following scalar equation:

$$S(x, y, z, t) = 0 \tag{1}$$

such that the function S, which possesses almost everywhere first order partial derivatives, acquires nonzero values at all points not lying on the interface [23]. The function S satisfies the differential

equation:

$$\frac{\partial S}{\partial t} + \mathbf{v_e} \cdot \nabla S = 0 \tag{2}$$

where $\mathbf{v_e} = \Omega_e J_e \mathbf{n}$ is the surface local normal velocity , with Ω_e the solid molar volume of phase e, J_e the molar rate of ablation, and $\mathbf{n} = \nabla S / \|\nabla S\|$ the normal pointing outwards from the surface [23]. For an analytical resolution, S can be rewritten under a more convenient explicit form like: $S = z - f(x, y, t)$. However, it requires the function $z = f(x, y, t)$ to be single-valued. For example, the latter condition is not satisfied on vertical walls. Nevertheless, it is shown in subsection 4.4.4 that in some trivial cases the knowledge of the partial derivatives of f enable an extrapolation of S even if f is not single-valued.

The chemical balance of the oxidation process under dry air at atmospheric pressure and at a controlled temperature of $898\,K$ writes [24]:

$$C_{(s)} + O_2 \rightleftharpoons CO_2 \tag{3}$$

In the conditions described above, this reaction is thermodynamically promoted since $\Delta_f G^\circ(CO_2) = -395\,kJ \cdot mol^{-1}$. The equilibrium partial pressures of reactants and products are in the ratio : $P_{CO_2}/P_{O_2} = 10^{23}$ [24]. This implies that : (i) only the kinetic aspect of the reaction has to be taken into account, (ii) the reaction may be limited by a low partial pressure of O_2, noted C. Hence, J_e is given by a first order kinetic law [9]:

$$J_e = k_e\, C \tag{4}$$

where k_e is the reactivity, whose variation from one constituant to another will be responsible for structural roughness. The description of roughness acquisition involves the evaluation of $\mathbf{v}$ at any point of the interface. This requires knowledge of the wall concentration which arises from a competition between consumption and mass transport in the bulk fluid phase. For the experimental conditions of this study, the thickness of the dynamic boundary layer δ (see figure 2-a) is $1.7\,mm$, and oxygen transport can be modeled by pure diffusion in this zone [9]. Therefore, mass conservation for oxygen writes:

$$\frac{\partial C}{\partial t} + \nabla \cdot (-D \nabla C) = 0 \tag{5}$$

where D is the bulk diffusion coefficient of O_2 in air.

The modeling strategy is based on ideas arising from the analysis of the samples. The onset of surface roughness and the global recession are modeled using two changes of scale: (i) microscopic scale (fiber (f), intra-bundle matrix (m), interphase (i)) to mesoscopic scale (bundle) (see figure 2-b-c) and (ii) mesoscopic scale (bundle, inter-bundle matrix) to macroscopic (composite) scale (see figure 2-a). The input values are then the intrinsic properties of fibers and matrices.

4 Mesoscopic scale analytical model

The 3D C/C composite is made of four mesoscopic components : matrix octets, inter-bundle interphase, parallel bundles (parallel to surface), and perpendicular bundles (perpendicular to surface). Matrix octets and inter-bundle interphase are bulk homogeneous materials whose reactivities have to be experimentally measured. The behavior of the parallel bundles cannot be inferred in steady state since they undergo layer-by-layer ablation, as represented on figure 2-c. Fortunately they are shown to display no influence on the composite overall behavior in steady state (see subsection 5). Consequently, this section focuses on perpendicular bundle modeling.

4.1 Extra hypotheses and boundary conditions for perpendicular bundles

There are two kinds of extra hypotheses as compared to the general model: the first ones are on the material architecture, the second ones are on the physical phenomena. Concerning the first ones, inside the bundle, the fibers are assumed homogeneous, isotropic, perpendicular to surface, axi-symmetrical, and surrounded by an isotropic homogeneous interphase. As represented on figure $3-b$, the height of the bulk matrix (h_m) is at any time lower than that of the fibers (h_f) – or at most equal. The hypotheses on the physical phenomena are : (i) a steady state is reached, (ii) the interphase surface remains flat and perpendicular to the $\mathbf{z}$ axis (see figures 3-b and c). A previous numerical work has shown that these hypotheses were correct [15]. Moreover, it is assumed that in steady state the gradient of reactant concentration is unidirectional along $\mathbf{z}$, that is, mass transfer is perpendicular to the overall surface. The validity of this hypothesis is studied *a posteriori* at the end of subsection 4.4 by computing the diffusion/reaction problem on the obtained analytical geometries (see figure 4). This vertical flux hypothesis has two main interests for the analytical modeling: first, the concentration profile at any point of the cell can be straightforwardly derived from a 1-D resolution of the model in steady state (see subsection below); second, it enables to address separately fiber and bulk matrix recession in a 3D C/C (as mass transfer is then decoupled for these two phases). This second point, added to the fact that $h_m < h_f$, means that the intra-bundle matrix has no effect on the 3D C/C bundle behavior (see subsection 4.6). Therefore, cell b of figure 3 can be simplified into cell c, boundary conditions relative to the model domain being: (i) on boundary layer top: a Dirichlet condition ($C = C_0$), (ii) on the lateral boundaries: symmetry conditions.

4.2 Concentration field and ablation velocity

Let the concentration field be determined using the vertical mass transfer hypothesis. A simple approach is possible on a receding flat surface in steady state, solving the model presented above in that particular case. Since the interphase contains the lower part of the overall surface, the knowledge of the concentration above it provides the concentration in the whole fluid phase. The interphase surface S_i can be

described by: $S_i(z,t) = h(t) - z = 0$. Let $v_a = \partial h/\partial t$ be the ablation velocity in steady state. Then, using the notations of figure $3-c$, equation (2) applied to S_i gives:

$$v_a = -\Omega_i k_i C_i \tag{6}$$

where $C_i = C(z = 0)$. Assuming a vertical concentration gradient and steady state, the integration of equation (5) gives $C(z)$ at each point of the fluid phase:

$$C(z) = C_i + \frac{C_0 - C_i}{h_f + \delta_c} z \tag{7}$$

with $C_i = C_0/(1 + Da_i)$, where $Da_i = k_i(h_f + \delta_c)/D$ is a Damköhler number. The normalized ablation velocity $\widehat{v_a} = v_a/(-\Omega_i k_i C_0)$ is a function of Da_i. For $Da_i < 0.01$, the diffusion velocity is large compared to the reactivity, that is, the regime is reaction-limited; hence, concentration is equal to C_0 in the whole fluid phase and $\widehat{v_a}$ tends to one. In the converse case, the regime is diffusion-limited ($Da_i > 100$): the concentration close to the wall and $\widehat{v_a}$ tend towards zero. Between these two limits, the regime is called intermediate or mixed : the concentration value on the wall (as well as the normalized ablation velocity) stems from the competition between reaction and diffusion.

4.3 Differential equation of fibers surface

Two resolution methods are provided.

4.3.1 First method

As represented on figure 3-c, the surface of an axi-symmetric fiber stripped by ablation can be described by the following equation in cylindrical coordinates: $S_f(r,\theta,z,t) = r - R(z,t)$. Substituting the derivatives in cylindrical coordinates of S_f in equation (2), one obtains :

$$-\frac{\partial R}{\partial t} + \Omega_f J_f(z)\sqrt{\left(\frac{\partial R}{\partial z}\right)^2 + 1} = 0 \tag{8}$$

where

$$\frac{\partial R}{\partial t} = \frac{\partial R}{\partial z}\frac{\partial z}{\partial t} = \frac{\partial R}{\partial z} v_a \tag{9}$$

and where $J_f(z) = -k_f C(z)$. Combining these results with the results of the unidirectional concentration gradient, $R(z)$ is found to be given in steady state by the following differential equation :

$$\frac{dR}{dz} = -\frac{1 + \frac{z}{\mathcal{L}}}{\sqrt{A^2 - \left(1 + \frac{z}{\mathcal{L}}\right)^2}} \tag{10}$$

where $A = (k_i\Omega_i)/(k_f\Omega_f)$ and $\mathcal{L} = D/k_i$ are respectively a dimensionless number and a characteristic length of ablation. Equation (10) is defined only for $z \in [0, \mathcal{L}(A-1)[$. As sketched on figure 3-c, the boundary condition for integration is $R(z=0) = R_f$.

Note that equation (10) features the first non trivial result : the value of C_0 and the size of the concentration boundary layer δ_c have no influence on the material behavior in terms of surface roughness, whereas they are shown to strongly affect the ablation velocity (equations (6) and (7)).

4.3.2 Second method

This second method provides a more concrete understanding of equation (10). Let the fiber tip surface be given by the function $R(z)$, represented on figure $3-c$. In steady state, the interphase recession along $\mathbf{e_z}$ is v_a at $z = 0$, while at this ordinate the fiber recession along $\mathbf{e_z}$ is necessarily null, since the fiber is protected by the interphase. In other words, in a moving referential of velocity $v_a\,\mathbf{e_z}$ (note that $v_a < 0$), the interphase would seem static while the fiber would appear emerging from the interphase surface at a velocity $-v_a\,\mathbf{e_z}$. The steady state is made possible because the fiber is progressively ablated along $\mathbf{e_r}$ until it disappears ($R(z) = 0$ for some z). Then, as represented on figure $3-c$, the value of $R(z + dz)$ is smaller than the value of $R(z)$, since it has been submitted to an ablation along $\mathbf{e_r}$ during an additional duration dt. In steady state, this duration is given by the vertical ablation velocity : $dt = dz/(-v_a)$. The horizontal ablation velocity $v_r(z)$ on the fiber is given by the projection on $\mathbf{e_r}$ of the recession velocity (along $\mathbf{n}$):

$$v_r = -\frac{\Omega_f k_f C(z)}{cos(\gamma)} \tag{11}$$

where $\gamma = (\mathbf{e_r}, \mathbf{n})$. Then, in steady state, the increment of R between z and $z + dz$ writes:

$$R(z + dz) \; - \; R(z) \; = \frac{\Omega_f k_f C(z)}{v_a cos(\gamma)}\, dz \tag{12}$$

Standard trigonometry gives:

$$\frac{1}{cos(\gamma)} \; = \sqrt{1 + \left(\frac{dR}{dz}\right)^2} \tag{13}$$

Summing up, one has :

$$\frac{R(z + dz) - R(z)}{dz} = \frac{dR}{dz} = \frac{\Omega_f k_f C(z)}{v_a} \sqrt{1 + \left(\frac{dR}{dz}\right)^2} \tag{14}$$

Combining this result with equation (7), equation (10) is obtained again.

4.4 Solutions

First, the limiting cases are studied, then equation (10) is solved in the general case and interpreted in terms of physical fiber surface.

4.4.1 Reaction-limited regime

A reaction-limited regime is attained when the reactivity is low compared to mass transfer. Hence, the concentration in the fluid phase is equal to C_0 everywhere. In the present case, the mass transfer being restricted to pure diffusion, it means that $\mathcal{L}$ tends to infinite, or at least is large compared to any

characteristic length of the problem. Then, with $\mathcal{L} >> z$, equation (10) can be simplified :

$$\frac{dR}{dz} = -\frac{1}{\sqrt{A^2-1}} \tag{15}$$

The integration of equation (15) with the boundary condition $R(z=0) = R_f$ gives the fiber geometry for a reaction-limited regime:

$$R(z) = R_f - \frac{z}{\sqrt{A^2-1}} \qquad \text{with} \qquad z \in [0, R_f\sqrt{A^2-1}] \tag{16}$$

The fiber is then a cone of height $h_f = R_f\sqrt{A^2-1}$ (see figure 5-a-α). This result is in accordance with the work of Glime and Cawley [25], who addressed analytically the reaction-limited regime using another approach.

Substituting $C_i = C_0$ into equation (6), the ablation velocity is found to be driven only by the interphase:

$$v_a = -\Omega_i k_i C_0 \tag{17}$$

This result has an implication for material fabrication. In the applications for which ablation is limited by the reaction (quite often), it is useless trying to improve the strong phases as far as a steady-state regime is attained. The interphase has definitely to be improved first.

4.4.2 Diffusion-limited regime

In the converse case, when the reactivity is low compared to mass transfer, a diffusion-limited regime establishes. $\mathcal{L}$ tends to zero. Since A is limited (for obvious physical reasons), the definition domain of equation (10) shrinks to an empty set. Indeed, the problem becomes 1-D : the wall remains flat, no surface roughness appears (see figure 5-a-ζ). Combining equations (6-7) for $h_f = 0$ and $L_a \to 0$, the recession velocity in diffusion-limited regime writes :

$$v_a = -\frac{\Omega_i C_0 D}{\delta_c} \tag{18}$$

Hence, this case is well described by the 1-D problem for $Da_i > 100$; the ablation velocity no longer depends on the oxidation reactivity.

4.4.3 Trivial cases

When $A = (k_i\Omega_i)/(k_f\Omega_f)$ tends to 1, or R_f tends to zero, the problem also turns out to be 1-D [15]. Then, in the following, it is assumed that $A > 1$ and $R_f > 0$.

4.4.4 General case

The integration of equation (10) gives the equation of the fiber surface :

$$R(z) = \mathcal{L}\left(\sqrt{A^2 - \left(1+\frac{z}{\mathcal{L}}\right)^2} - \sqrt{A^2-1}\right) + R_f \tag{19}$$

with $z \in [0, \mathcal{L}(A-1)[$ and $R(z) \geq 0$.

Note that if $R_f/\mathcal{L} \geq \sqrt{A^2-1}$ then $R(\mathcal{L}(A-1)) > 0$ and $\lim_{z\to\mathcal{L}(A-1)}(\frac{dR}{dz}) = -\infty$, *i.e.* the slope at this point is horizontal. The surface S_f, which is no longer single-valued, has to be extrapolated using this limit. The value of the derivative tends to support the idea that the fiber tip exhibits a plateau and its height is limited, with $h_f = \mathcal{L}(A-1)$. One has then to verify that the steady state is possible under this hypothesis. The equality between the recession velocity of the fiber on the plateau (v_z^f) and on the interphase (v_a) is to be obtained for the fiber height $h_f = \mathcal{L}(A-1)$. Combining equations (6) and (7), the recession velocity on the plateau of the fiber is found to be:

$$v_z^f = \Omega_f k_f C_0 \frac{1 + Da_i h_f/(h_f + \delta_c)}{1 - Da_i} \tag{20}$$

It is shown to be equal to v_a for a unique value of h_f, which is the previously found value $h_f = \mathcal{L}(A-1)$. The surface S_f has then to be extrapolated by a plateau (see figure 5-a-ϵ).

Since R_f is strictly positive, equation (19) can be rewritten in a more convenient dimensionless form :

$$\widetilde{R}(\widetilde{z}) = Sh^{-1}\left(\sqrt{A^2 - (1+Sh\,\widetilde{z})^2} - \sqrt{A^2-1}\right) + 1 \tag{21}$$

where, $\widetilde{R} = R/R_f$, $\widetilde{z} = z/R_f$, and $Sh = R_f/\mathcal{L} = R_f\,k_i/D$ is a Sherwood number, and with the condition $\widetilde{z} \in [0, (A-1)/Sh[$. This is the equation of a circle arc (sphere segment) with center at $(\widetilde{R} = 1 - \sqrt{A^2-1}/Sh; \widetilde{z} = -1/Sh)$ and radius A/Sh.

The reduced height $\widetilde{h} = h_f/R_f$ is an explicit function of A and Sh:

$$\widetilde{h} = \sqrt{Sh^{-2} + 2Sh^{-1}\sqrt{A^2-1} - 1} - Sh^{-1} \tag{22}$$

with $Sh < \sqrt{A^2-1}$, leading to an ogival fiber. In the converse case, as explained above, the fiber tip features a plateau and $\widetilde{h} = (A-1)/Sh$.

For $Sh < \sqrt{A^2-1}$, the angle at the tip of the fibers α_f is found to be:

$$\alpha_f = 2\,Arctan\left(-\frac{\partial\widetilde{R}}{\partial\widetilde{z}}(\widetilde{z}=\widetilde{h})\right) = 2\,Arctan\left(\frac{1+2\widetilde{h}\,Sh}{\sqrt{A^2 - \left(1+\widetilde{h}\,Sh\right)^2}}\right) \tag{23}$$

The above analytical results are based on a vertical diffusion flux hypothesis. As represented on figure 4 for $Sh = 1$, and $A = 5$, the validity of this hypothesis has been verified in 3D (2D axisymmetrical computational cell) using finite element modeling. The reaction/diffusion problem has been solved on the analytical geometries in all regimes (i.e, for values of Sh between 0.001 and 1000). A validation of the hypothesis is obtained with a certainty equal to the computing precision in all the cases.

4.5 Parameter variation and analysis

The emerging fiber morphology, given by equation (21), is a function of the Sherwood number Sh and the contrast of the intrinsic oxidation rates A. The Sherwood number is an indicator of the regime : if it tends to infinite, the recession is controlled by diffusion and there is no roughness (see figure 5-a-ζ); if it

tends to zero, reaction controls recession, and the surface roughness is maximal (conical fibers : see figure 5-a-α); between these two limits the regime is intermediate (ogival fibers, possibly with a plateau: see figures 5-a-α to 5-a-ϵ). The number A is an indicator of the reactivity and density contrast between the fiber and the interphase. The higher it is, the higher $\widetilde{h}$ is, as soon as the mass diffusion process does not bring a limitation. In reaction-limited regime, when A is large, the increase of $\widetilde{h}$ is almost linear with A, as represented on figure 6 which has been plotted using equation (22). Indeed, for $A >> 1$, equation (16) gives $\widetilde{h} \sim A$. However, in diffusion-limited regime, A has no effect on the bundle behavior (see equation (18) and figure 6). In the intermediate regime, the evolution of $\widetilde{h}$ and of the fibers morphology versus A is no longer linear : the bundle behavior is a complex mixture law resulting from the competition between diffusion and reaction.

Figure 5-b shows fiber geometries for various values of A for a constant ratio $A/Sh = 10$. In other words, it is a parameter variation on k_i, whereas other variables are taken constant. This figure tends to temper the widespread idea that the interphase controls the oxidation when the composite seems to lie in reaction-limited regime. Indeed, as represented on this figure, the interphase seems to play a great role because it recedes first and because the fibers become sharp. The figure shows well that the increase of A (that is, of k_i) has a great influence on the bundle behavior when A is low. However, when A becomes larger, its influence decreases until it disappears : for values of A higher than 500 the fiber morphology does not change any more (figure 5-b). This is due to a limitation by diffusion on the interphase, while the fiber tip is still in reaction-limited regime. Then, the interphase is fully protected by the fiber.

Reciprocally, the analysis of the morphology of a fiber should enable to assess, by inverse analysis, the values of A and Sh. Indeed, the evaluation of the two geometrical parameters α_f and h_f are sufficient to determine A and Sh. Such an inverse analysis can be straightforwardly done on an analytical plot of the fiber geometry. However, the experimental evaluation of α_f is difficult, or even impossible in certain cases [17]. Then, the effective reactivity, which is experimentally easier to determine, may be used as a second experimental parameter.

4.6 Effective reactivity

The effective reactivity k_{eff} is used by engineers to assess the ablation velocity of a material, assumed homogeneous, through the following relation:

$$v_a = -\Omega_{eff} k_{eff} C_w \tag{24}$$

where Ω_{eff} is the averaged molar volume of the material, and C_w the concentration in oxygen on the homogeneous material flat surface. To extend this study to the assessment of a consistant effective reactivity, the notion of surface for a heterogeneous material featuring a rough surface has to be defined. Also, two changes of scale are useful to determine the effective reactivity of a 3D C/C composite from the prop-

erties of its microscopic components: (i) micro-scale (fiber) to meso-scale (bundle) and (ii) meso-scale (bundle) to macro-scale (composite). In the present section, the first change of scale is addressed.

The composite behavior in terms of surface roughness at mesoscopic scale has been shown not to depend on δ_c and C_0; then, the effective reactivity of the bundle can be assessed using any value of δ_c. To facilitate the next change of scale, it is chosen to assess the effective reactivity at the height h_f ($\delta_c = 0$) using a formal concentration on the apparent wall $C_w = C(z = h_f)$. Note that the concentration on the wall C_w may be determined at macroscopic scale (see subsection 5), just as $C(z)$ is determined at mesoscopic scale. The idea is then to replace the volumic cell of figure 3-c by an equivalent reactive and recessive surface placed horizontally at ordinate $z = h_f$. The aim of this change of scale is to infer by homogenization a homogeneous material whose surface would have the chemical properties of the actual rough bundle. This would provide : (i) a phenomenological law giving the effective properties of the bundle combining those of its components, (ii) input values for the model at macroscopic scale. The ablation velocity of a representative elementary surface (RES) of the bundle writes:

$$\begin{cases} v_{a,b} = -\Omega_b k_b C_w \\ \Omega_b = (\varepsilon_f/\Omega_f + \varepsilon_i/\Omega_i + (1-\varepsilon_i-\varepsilon_f)/\Omega_m)^{-1} \end{cases} \tag{25}$$

where k_b is the effective reactivity of the bundle, and Ω_b the solid molar volume of the bundle, with ε_i the volume fraction of phase i. This change of scale has to take into account the actual architecture of the composite. That is why the notion of RES is introduced here, though the model is applicable to any fiber of the bundle. The RES must be large enough to be representative of the actual homogenized quantity: $\Omega_b k_b$. Indeed, one notes a non negligible standard deviation in the measurement of the fiber bundles properties [17]. The value of Ω_b is directly connected to these local variations. The value of k_b is indirectly linked to these variations via the variations of k_i, k_f, R_f. Then, the size of the RES has to be large in front of these local variations, which are of the order of a fiber diameter. The homogenized quantity $\Omega_b k_b$ may then be associated to a representative surface of approximatively ten fiber diameters square. However, the bundle itself may be subject to morphological variations (see section 5). Consequently, the RES must be elementary, that is, small with respect to the size of the phenomena that take place on the bundle. Section 5 shows that the size to take into account is the bundle section of width l. Hence, one has to verify $l < 100\,(2R_f)$. For the material of this study, these sufficient conditions to address the change of scale are satisfied.

Let us define $\widetilde{R}_b^{eff}$ the ratio of the effective ablation velocity of a bundle $v_{a,b}$ to the ablation velocity of the interphase v_i. For a given wall concentration, and combining equations (6), (7), (22) and (25), $\widetilde{R}_b^{eff}$

is obtained:

$$\widetilde{R}_b^{eff} = \begin{cases} \left(1 + 2Sh\sqrt{A^2-1} - Sh^2\right)^{-1/2} & \text{if} \quad 0 \leq Sh < \sqrt{A^2-1} \\ 1/A & \text{if} \quad Sh \geq \sqrt{A^2-1} \end{cases} \tag{26}$$

$\widetilde{R}_b^{eff}$ is a convenient normalized form to express the effective reactivity associated to a RES of the bundle because it is only a function of A and Sh. The effective reactivity can then be easily obtained from the knowledge of $\Omega_i k_i$ and Ω_b. $\widetilde{R}_b^{eff}$ is plotted on figure 7. For given values of $\Omega_i k_i$ and Ω_b, the effective reactivity decreases with the increase of A and Sh. Indeed, A increases the strength of the fibers, which thus tend to protect the interphase provided the regime is not limited by reaction (as discussed in the above subsection). When Sh is high, the ablation is limited by reaction (conical fibers), and then, considering $\Omega_i = \Omega_b$, the effective reactivity is that of the interphase. When Sh becomes larger, after a transition to a mixed regime (ogival fibers), the ablation become limited by diffusion (no surface roughness) and the effective reactivity decreases. As a conclusion, this theoretical analysis reinforces the widespread idea, arising from experimental observations, that the effective ablation velocity of the composite cannot be modeled using a simple arithmetic average of the ablation velocities of its components [1, 9, 12].

4.7 Comparison of the results with two previous numerical works

The model has been solved recently in 3-D using a homemade simulation code based, among others, on random walks (diffusion) and an efficient surface description (moving reactive interface) [15, 26]. A parametrical study has been carried out on the fibers morphologies in steady state [15]. The conclusions are in correct agreement with the analytical geometries presented above.

The model was first numerically solved in 2-D in 1995 [27], using a finite difference scheme, with the following values : $k_f = 2.10^{-4}\, m \cdot s^{-1}$, $k_i = 4.10^{-3}\, m \cdot s^{-1}$, $\Omega_f = \Omega_i$, $R_f = 33\, \mu m$, and $D = 2.10^{-4}\, m^2 \cdot s^{-1}$. Then, one has : $A = 20$, and $Sh = 6.6\, 10^{-4}$. Hence the regime is very close to the reaction-limited regime : oxidation is mainly driven by the interphase. Using equations (21) and (22), the fiber geometry can be assessed as conical with $\widetilde{h} \simeq 19.9$. The value for $\widetilde{h}$ numerically obtained in [27] is about 18. The error, around 10%, is likely to arise from some numerical approximations. In particular, the interface description, using a quadrangular approximation, may have introduced uncertainties in the resolution, as the orientation of the interface is shown to play a role in the onset of surface roughness [23] (see section 4.3). In the discussion of [27], it is underlined that the recession of the highly oxidizable layers slows down modestly with time, as the oxygen concentration at the bottom of the crevice is reduced. Indeed, according to equation (26), due to the protection of the interphase by the fiber, the ablation velocity decreases by 1.3% in steady state. As a conclusion, the above analytical results are also in agreement with the numerical study presented in [27].

5 Macroscopic scale analytical model

In this section, the second change of scale is addressed : the steady state behavior of the composite is inferred from that of its mesoscopic components.

5.1 Hypotheses

At macroscopic scale, perpendicular bundles can be assumed homogeneous, isotropic, strictly perpendicular to surface, and having a square section surrounded by an interphase ($i-b$). Let the first two non-trivial hypotheses be discussed. As represented on figure 8-a, whose notations and associated model are depicted in the following subsection, in steady state the perpendicular bundle tips are sharp, like the fibers. Then, the local normal $\mathbf{n}$ to the elementary surface $dS(z)$ features an angle γ_b with the horizontal. As represented on figure 8-b, and justified in subsection 4.6, the bundle surface is actually defined by the tips of the fibers. Moreover, according to equation (2), the local surface recession occurs along $-\mathbf{n}$. In consideration of the small size of the RES as compared to the bundle section, the local concentration on the wall $C_w(z)$ at ordinate z for a RES may be considered as constant. Then, the local 3-D cell can be represented by the scheme of figure 8-c. The associated model is the same as for the mesoscopic scale, except that the fibers are tilted of an angle $\pi/2-\gamma_b$. This problem has been numerically solved for various angles in transient regime in [17]. The two main conclusions are : (i) steady state is always reached, (ii) the effective ablation velocity is not a function of γ_b. In other words, the effective ablation velocities obtained analytically for perpendicular fibers are usable for any orientation. Moreover, this result shows the accuracy of the assumption according to which the bundle could be considered as homogeneous and isotropic at macroscopic scale. The bundles section is square, and the interphase associated to the perpendicular bundle is a pitch-based graphitized matrix, which constitutes an interphase between the perpendicular bundles and either the bulk inter-bundle matrix or the parallel bundles. Figure 1 shows that both the bulk inter-bundle matrix and the parallel bundles appear lower than the perpendicular bundles, but higher than the interphase. The interphase is assumed homogeneous, isotropic, flat, and smooth.

The hypotheses on the physical phenomena are : (i) the steady state is reached at all scales, (ii) vertical concentration gradient, (iii) the interphase surface associated to the bundles can be modeled by a flat surface perpendicular to the $\mathbf{z}$ axis, and (iv) the duration of the transient regime at mesoscopic scale is negligible compared to that at macroscopic scale.

5.2 Equation of perpendicular bundles surface

Under the above hypotheses, the macroscopic scale model is equivalent to that of the mesoscopic scale. This is represented on figure 8-a, where $\delta_{c,b}$, $C_{0,b}$ and h_b are the respective counterparts for the bundle of

δ_c, C_0 and h_f for the fiber. However, this time, the surface of a perpendicular bundle stripped by ablation features a square cross-section of dimension l, $l/2$ being the homologue of R_f. Naturally, the geometry of a square-section bundle is more efficiently described in cartesian coordinates : $S_b(x,y,z,t) = z - F(x,y,t) = 0$. The equation of the surface $z = F(x,y)$ in steady state can be derived using the method developed in subsection 4. One notices that in equation (2) the gradient along $\mathbf{e_r}$ in cylindrical coordinates is equivalent to both gradients along $\mathbf{x}$ and $\mathbf{y}$ in cartesian coordinates. Then, the results of the mesoscopic scales can be converted to macroscopic scale. Hence, substituting suitable notations in equation (22), $z = F(x,y)$ writes in cartesian coordinates:

$$z = min(f(x), f(y)) \quad \text{with} \quad (x,y) \in [-l/2, l/2]^2 \quad \text{where}$$
$$f(u) = \begin{cases} \mathcal{L}_b \left(\sqrt{A_b^2 - \left((|u| - l/2)/\mathcal{L}_b + \sqrt{A_b^2 - 1} \right)^2} - 1 \right) & \text{if} \quad l < 2\,\mathcal{L}_b \sqrt{A_b^2 - 1} \\ \mathcal{L}_b \,(A_b - 1) & \text{if} \quad l \geq 2\,\mathcal{L}_b \sqrt{A_b^2 - 1} \end{cases} \tag{27}$$

where $\mathcal{L}_b = D/k_{i-b}$ is a length associated to the perpendicular bundle and $A_b = (k_{i-b}\Omega_{i-b})/(k_b\Omega_b)$ is the ratio between the gasification rates of the interphase surrounding the bundle and the bundle itself.

5.3 Discussion

According to this model, the perpendicular bundles should emerge from the interphase surface and adopt a pyramidal geometry if diffusion is not limiting. Let the Sherwood number associated to the bundles be: $Sh_b = l/(2\mathcal{L}_b) = l\,k_{i-b}/(2D)$. The morphology of a square-section bundle is represented as a function of Sherwood number for $A_b = 5$ on figure 9. Obviously, the evolution of the bundle morphology with the physico-chemical parameters is comparable to that of the fibers, since the model is the same. Nevertheless, note that in the general case $Sh_b >> Sh$ and $A_b \neq A$; then in a C/C composite, the macroscopic scale behavior may differ from the mesoscopic scale behavior. For instance, the regime may be reaction-limited at mesoscopic scale, while it could be intermediate at macroscopic scale.

5.4 Effective behavior of the composite in steady state

Equation (27) shows that the macroscopic behavior is independent of $\delta_{c,b}$ and $C_{0,b}$. The second change of scale can then be addressed using the method developed for the first change of scale with bundle tips standing in for fiber tips. By properly rewriting equation (26), the normalized effective ablation velocity of the composite $\widetilde{R}_C^{eff} = (\Omega_C k_C)/(\Omega_{i-b} k_{i-b})$ writes :

$$\widetilde{R}_C^{eff} = \begin{cases} \left(1 + 2Sh_b\sqrt{A_b^2 - 1} - Sh_b^2\right)^{-1/2} & \text{if} \quad 0 \leq Sh_b < \sqrt{A_b^2 - 1} \\ 1/A_b & \text{if} \quad Sh \geq \sqrt{A_b^2 - 1} \end{cases} \tag{28}$$

The plot of such a function is represented on figure 7 and commented in subsection 4.6, except that the variables are now R_C^{eff}, Sh_b, and A_b instead of R_b^{eff}, Sh, and A.

6 Validation

Independent measurements of the intrinsic oxidation reactivities of the available composites components, that is, the ex-PAN fibers ($k_f \simeq 1.2\,10^{-5}\,m{\cdot}s^{-1}$) have also been carried out in the oxidation reactor under the experimental conditions described in section 2.1 [9, 17]. Unfortunately, the interphases associated to the bundles and to the fibers are not available as such: their oxidation reactivities cannot be evaluated by independent measurements. In the following, they are evaluated using the model and the analysis of the surface roughness. Even though this evaluation is done using the model, the validation is possible because surface roughness may be considered as an additional independent input value, which stands in for the oxidation reactivities of the interphases. The oxidation reactivity of the composite in steady state lies around $k_C^{eff-exp} = 3\,10^{-3}\,m \cdot s^{-1}$ [9, 17]. The procedure for the validation is firstly to assess the effective reactivity of the composite from the reactivity of the fibers, the physical parameters, the surface roughness, and using the two change of scale. Secondly, the effective oxidation reactivity of the composite obtained using the model may be compared to the experimental value (see figure 10).

Let the effective reactivity of the bundle be evaluated from that of the fibers (first change of scale). The first step is to determine the Sherwood number associated to the fiber: $Sh = k_i R_f/D$. Knudsen diffusivity effects can be neglected [17]. Hence, the diffusion coefficient is obtained using the Chapman-Enskog relation [28] for oxygen in dry air at atmospheric pressure and $898\,K$: $D = 1.34\,10^{-4}\,m^2 \cdot s^{-1}$. It is possible to determine an upper bound for the Sherwood number: $Sh < k_C^{eff-exp} R_f/D \simeq 10^{-4}$. According to the theoretical analysis, this clearly shows that the ablation regime is reaction-limited. This is also in accordance with the observation of sharp conical fibers on figure 1-a_μ. Moreover, the surface roughness analysis shows the fiber height, h_f, is $111 \pm 6\,\mu m$ for a mean fiber radius R_f around $3.5\,\mu m$ [17], that is, $\widetilde{h} = h_f/R_f \simeq 32$. Then, the contrast in the oxidation rates, $A = (k_i\Omega_i)/(k_f\Omega_f)$, is obtained from figure 6, or more accurately from equation (22). One notes that A is equal to $\widetilde{h}$ in reaction-limited regime; then A also lies around 32. The effective ablation reactivity of the bundle is driven by the interphase in reaction-limited regime (equation (17)). When $Sh << 1$, equation (26) becomes $\widetilde{R}_b^{eff} = (\Omega_b k_b)/(\Omega_i k_i) = 1$. The effective reactivity of the bundle is then $k_b = A\,k_f\,(\Omega_f/\Omega_b)$. In the case of the 3D C/C composite, one can assume that $\Omega_f \simeq \Omega_b$. Hence, one has $k_b \simeq 3.8\,10^{-4}\,m \cdot s^{-1}$. It is now possible to determine the oxidation reactivity of the interphase: $k_i = k_i = A\,k_f\,(\Omega_f/\Omega_i) \simeq 3.8\,10^{-4}\,m \cdot s^{-1}$.

Let us address the second change of scale. The Sherwood number for the bundle, $Sh_b = lk_{i-b}/(2D)$, lies around 10^{-3}. $\widetilde{h}_b$ is estimated to be about 8. Then, one deduces $A_b = 8$ and $\widetilde{R}_C^{eff} = (\Omega_C k_c)/(\Omega_{i-b} k_{i-b}) = 1$ from equation (28). The effective reactivity of the composite assessed from the model is then $k_C^{eff-m} = A_b\,k_y\,(\Omega_b/\Omega_C)$. In the case of the 3D C/C composite, one can assume that $\Omega_b \simeq \Omega_C$. Hence, one has

$k_C^{eff-m} \simeq 3.1\,10^{-3}\,m \cdot s^{-1}$.

As a conclusion, using the model and only the fiber reactivity, the effective reactivity of the composite has been evaluated in steady state from the study of its surface roughness. Comparing experimental and computed values, the error in the prediction is found to be about 3% (see figure 10). Moreover, the correct agreement, which is obtained in the modeling of surface roughness features (conical pointed fibers, pyramidal bundles), supports the validity of the model.

7 Conclusion

The behavior of a 3D C/C composite during physico-chemical ablation has been modeled in steady state from the microscopic scale up to the macroscopic one, using two suitable changes of scale : (i) microscopic scale (fiber, intra-bundle matrix) to mesoscopic scale (bundle) and (ii) mesoscopic scale (bundle, inter-bundle matrix) to macroscopic scale (composite). First, the surface roughness features have been analyzed in order to provide guidelines for the modeling. Then a multiscale modeling strategy has been set up. Its physical bases mainly rely on a general model for receding surfaces under a first order gasification process coupled to mass transfer by diffusion. This model has been analytically solved at mesoscopic scale considering a simplified composite architecture. Due to the higher recession velocity of a thin interphase, the fibers are partially uncovered and acquire a needle shape. Only two parameters are necessary to describe the steady state surface roughness features of the bundle : the ablation rate contrast A between the weakest (interphase) and strongest (fiber) phases, and a Sherwood number Sh. The height of the stripped part of the fibers (peak-to-valley surface roughness) increases with A. The stripped part of the fibers is conical for low values of Sh (reaction-limited regime), ogival for Sh around unity (transition regime), and button shaped for high values of Sh (diffusion-limited regime). Whenever Sh is large with respect to A, no surface roughness is observed. The model has then been used to infer the effective reactivity of the bundle from that of its components. In reaction-limited regime, a weakest-link process occurs : the reactivity of the bundle is equal to that of the weakest phase (component molar volumes being considered equal). When diffusional effects appear, the matrix is somehow protected by the fibers and the effective reactivity progressively tends to that of the fiber, that is, its value in diffusion-limited regime. These results are consistent with some previous studies [15, 27] and help in their interpretation. At macroscopic scale, the mesoscopic model applies, considering square section bundles instead of cylindrical fibers, and inter-bundle matrix instead of intra-bundle matrix. It has been shown that the same set of equations was usable, except that the parameters had to be adapted to macroscopic scale (A_b, Sh_b). Consequently, the multi-scale behavior of the composite has been obtained. The results of the model have been validated by comparison to the experimental surface roughness and oxidation reactivities. Incidentally, during this validation, the intra-bundle and inter-bundle interphase reactivities, which cannot

be independently measured, have been deduced from a surface roughness analysis.

As a whole, the results of the steady state models may be useful for: (i) the prediction of the multi-scale surface roughness as a function of the physico-chemical parameters, (ii) the prediction of the effective reactivity of the composite from that of its components, (iii) the research of an ideally optimal material, (iv) the determination of the components properties from the analysis of surface roughness.

The immediate outlook is to address actual composite architectures and transient regime. A second step would be to extrapolate this oxidation model to other causes of ablation, like sublimation or thermomechanical erosion.

Acknowledgments

The authors wish to thank J.-F. Epherre, G. Duffa, and J.-M. Goyhénèche (CEA) for fruitful discussions. Snecma Propulsion Solide and DGA are acknowledged for a Ph. D. grant to Y. Aspa. The authors also wish to thank CNRS and CEA for financial support, especially for a Ph. D. grant to J. Lachaud.

References

[1] L. M. Manocha, E. Fitzer, Carbon reinforcements and C/C composites, Springer, 1998, pp. 1–342.

[2] J. Couzi, J. de Winne, B. Leroy, Improvements in ablation predictions for reentry vehicle nosetip, in: W. Berry and J. Maylaert (Eds.), Proceedings of the Third European Symposium on Aerothermodynamics for Space Vehicles, ESA, Noordwijk, The Nederlands, 1998, pp. 493–499.

[3] G. Duffa, G. L. Vignoles, J.-M. Goyhénèche, Y. Aspa, Ablation of C/C composites: Investigation of roughness set-up from heterogeneous reactions, International Journal of Heat and Mass Transfer 48 (16) (2005) 3387–3401.

[4] V. Borie, J. Brulard, G. Lengellé, An areothermochemical analysis of carbon-carbon nozzle regression in solid-propellant rocket motors, in: Proceedings of the 24^{th} AIAA/ASME/SAE/ASEE Joint Propulsion Conference, AIAA paper 88-3346, Boston, MA, USA, 1988.

[5] K. Kuo, S. Keswani, A comprehensive theoretical model for carbon-carbon composite nozzle recession, Combustion Science and Technology 42 (1986) 177–192.

[6] S. Pestchanyi, V. Safronov, I. Landman, Estimation of carbon fibre composites as ITER divertor armour, Journal of Nuclear Materials 329–333 (2004) 697–701.

[7] H. Würz, B. Bazylev, I. Landman, S. Pestchanyi, V. Safronov, Macroscopic erosion of divertor and first wall armour in future tokamaks, Journal of Nuclear Materials 307–311 (2002) 60–68.

[8] J. A. Keenan, G. V. Candler, Simulation of ablation in earth atmospheric entry, in: Proceedings of the 28^{th} Thermophysics conference, AIAA paper 93-2789, Orlando, FL, 1993.

[9] J. Lachaud, N. Bertrand, G. L. Vignoles, G. Bourget, F. Rebillat, P. Weisbecker, A theoretical/experimental approach to the intrinsic oxidation reactivities of C/C composites and of their components, Carbon 45 (2007) 2768–2776.

[10] G. Duffa, Ablation, Monograph, CEA, Le Barp, France, 1996, pp. 111–112.

[11] J.-M. Goyhénèche, G. L. Vignoles, G. Duffa, Homogénéisation thermique d'interfaces rugueuses. Principe et application à différentes rugosités périodiques, in: Congrès Français de Thermique, Société Française de Thermique, Vandœuvre, France, 2004, 6 p.

[12] J. Lahaye, F. Louys, P. Ehrburger, The reactivity of carbon-carbon composites, Carbon 28 (1) (1990) 137–141.

[13] M. R. Wool, Summary of experimental and analytical results, Tech. Rep. SAMSO-TR-74-86, Passive Nosetip Technology Program (PANT) (January 1975).

[14] Y. I. Dimitrienko, I. D. Dimitrienko, Effect of thermomechanical erosion on heterogeneous combustion of composite materials in high-speed flows, Combustion and flame 122 (2000) 211–226.

[15] J. Lachaud, G. L. Vignoles, J. M. Goyhénèche, J. F. Epherre, Ablation in C/C composites: microscopic observations and 3D numerical simulation of surface roughness evolution, Ceramic Transactions 191 (2006) 149–160.

[16] J. Lachaud, Y. Aspa, G. L. Vignoles, J.-M. Goyhénèche, Modélisation 3D de l'ablation thermochimique des composites C/C, in: Congrès Français de Thermique, Societé Française de Thermique, Vandœuvre, France, 1 (2006) 125–130.

[17] J. Lachaud, Simulation of ablation of carbon-based composites, PhD thesis n°3291, Bordeaux 1 University, France, 2006. In English.

[18] J. C. Han, X. D. He, S. Y. Du, Oxidation and ablation of 3D carbon-carbon composite at up to 3000°C, Carbon 33 (4) (1995) 473–478.

[19] J. Lachaud, Y. Aspa, G. Vignoles, J.-M. Goyhénèche, 3D modeling of thermochemical ablation in carbon-based materials: effect of anisotropy on surface roughness onset, in: M. Dinguirard, J. Kleiman (Eds.), Proceedings of the Tenth International Symposium on Materials in a Space Environment, ESA, Noordwijk, The Netherlands, Vol. SP-616, 2006, 10 p.

[20] W. Guo, H. Xiao, E. Yasuada, Y. Cheng, Oxidation kinetics and mechanisms of a 2D-C/C composite, Carbon 44 (2006) 3269–3276.

[21] D. Cho, B. I. Yoon, Microstructural interpretation of the effect of various matrices on the ablation properties of carbon-fiber-reinforced composites, Composites science and technology 61 (2001) 271–280.

[22] Y.-J. Lee, H. J. Joo, Investigation on ablation behavior of CFRC composites prepared at different pressures, Composites: Part A 35 (2004) 1285–1290.

[23] I. V. Katardjiev, G. Carter, M. J. Nobes, S. Berg, H.-O. Blom, Three-dimensional simulation of surface evolution during growth and erosion, Journal of Vacuum Science and Technology A 12 (1) (1994) 61–68.

[24] Chase MW. NIST-JANAF Thermochemical Tables (4th ed.). Journal of Physical Chemical Reference Data 14 (1985), p 628.

[25] W. H. Glime, J. D. Cawley, Oxidation of carbon fibers and films in ceramics matrix composites: a weak link process, Carbon 33 (8) (1995) 1053–1060.

[26] G. L. Vignoles, Modelling binary, Knudsen, and transition regime diffusion inside complex porous media, J. Phys. IV France C5 (1995) 159–166.

[27] W. H. Glime, J. D. Cawley, A. J. Eckel, The evolution of a non-planar oxidation front in receding carbon fibers, Ceramic Transactions 46 (1995) 1039–1047.

[28] R. C. Reid, J. M. Prausnitz, B. E. Poling, The properties of gases and liquids, 4th Edition, McGraw Hill Book Company, 1987, pp. 1–688.

List of Figures

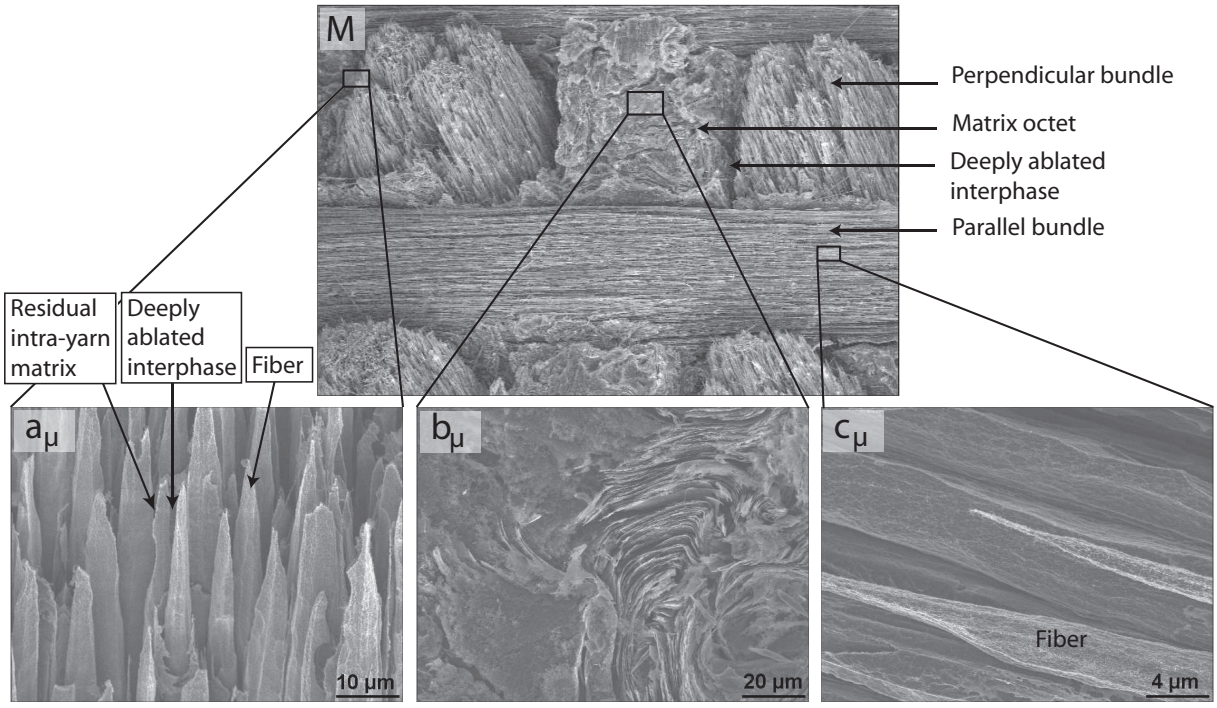

Fig. 1. SEM micrographs of 3D C/C surface after ablation in an oxidation reactor.

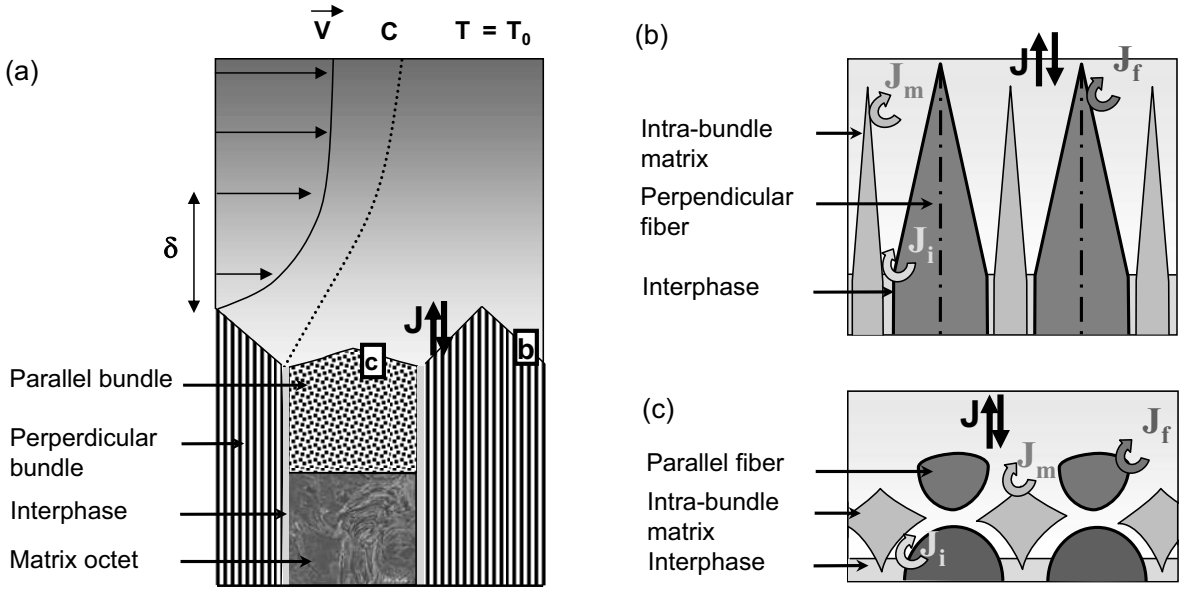

Fig. 2. Modeling strategy: sketch of the coupled phenomena on a 3D C/C during steady state ablation.

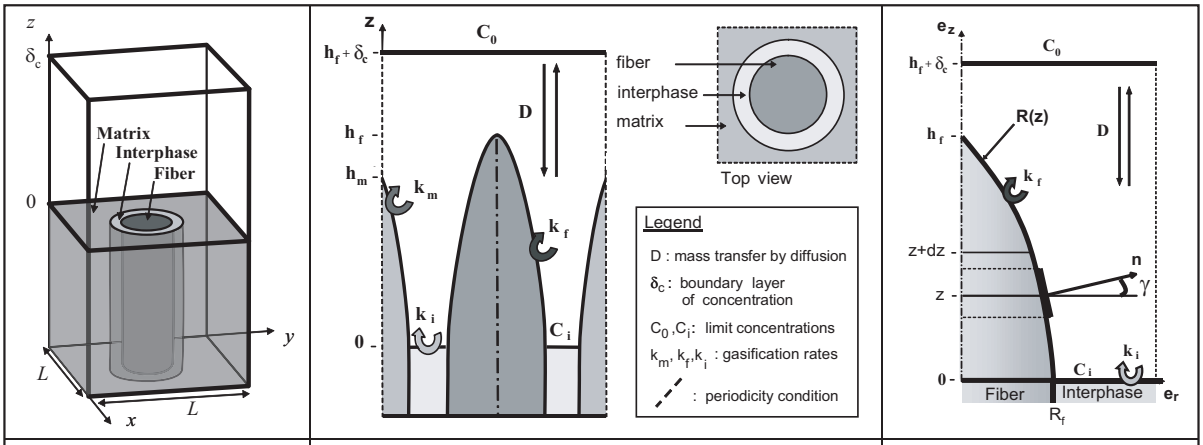

Fig. 3. Scheme of the elementary pattern and of the proposed model.

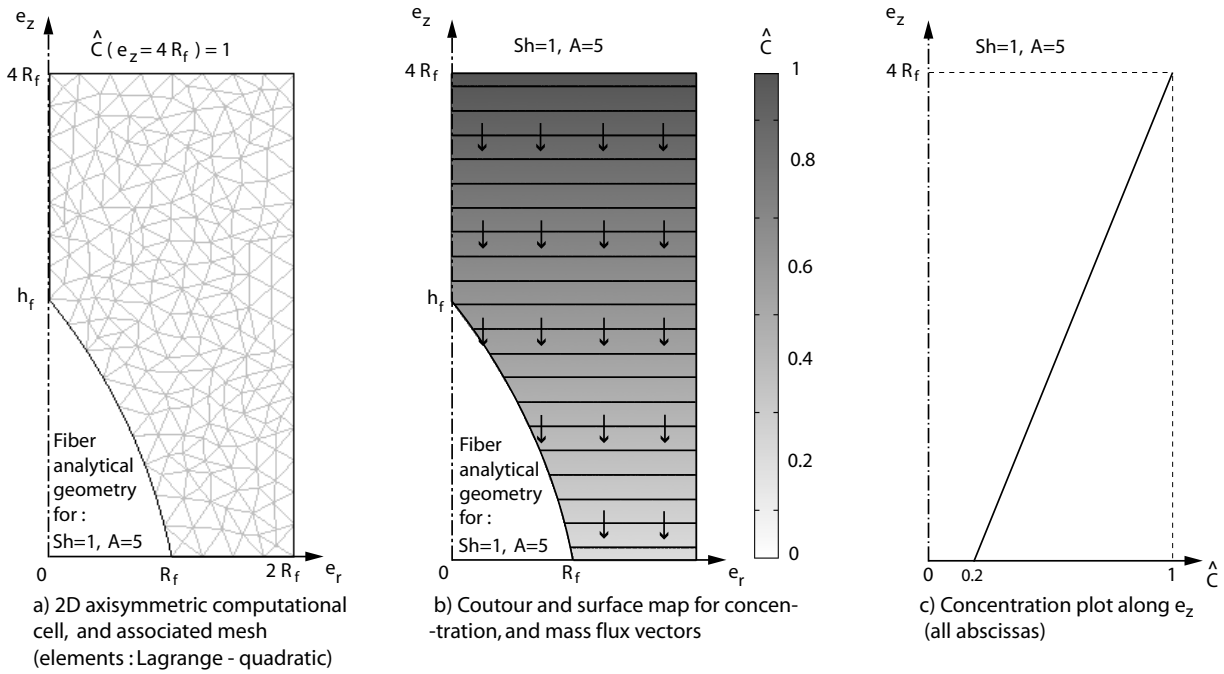

Fig. 4. Numerical validation of the vertical flux hypothesis.

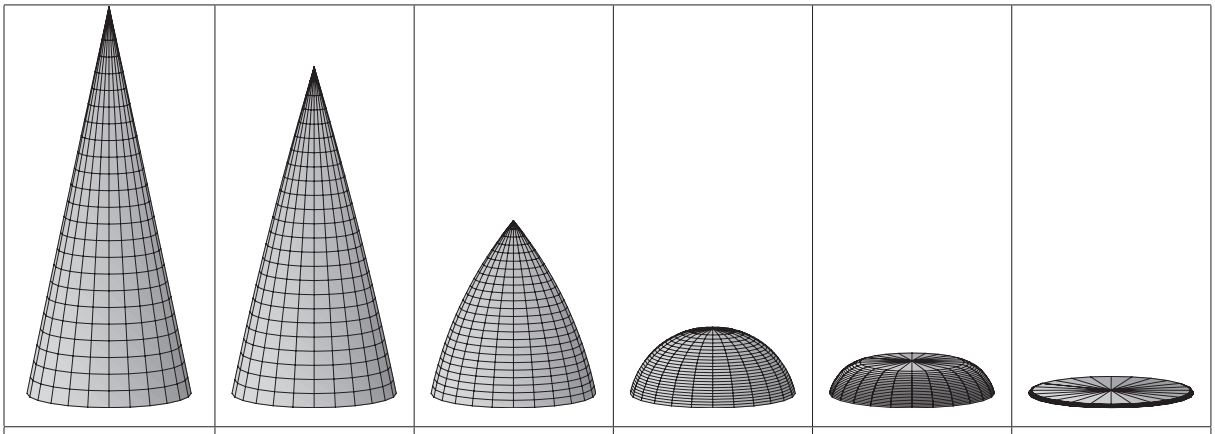

a) Fiber geometry as a function of *Sh* (with *A=5*)

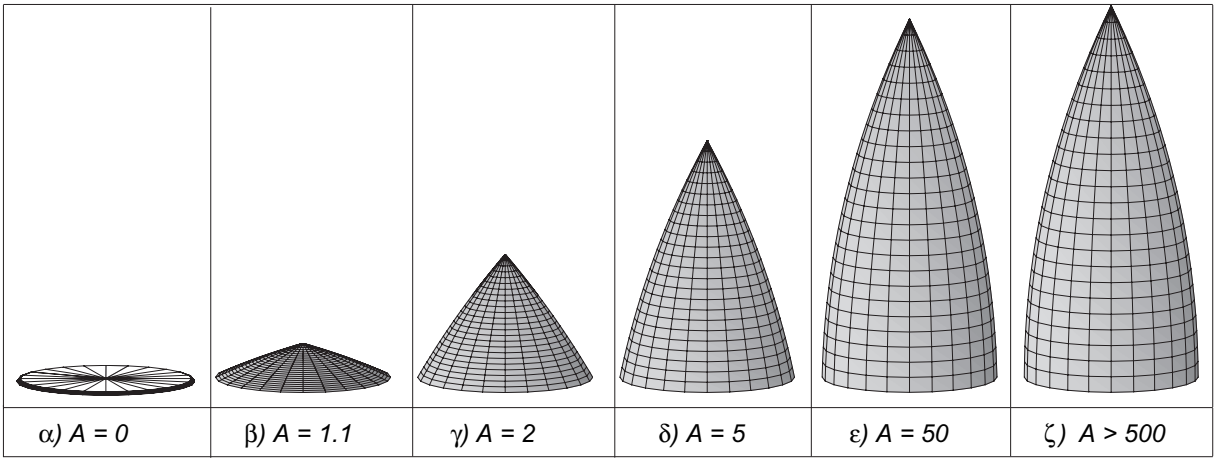

b) Fiber geometry as a function of *A* (with *A/Sh=10*)

Fig. 5. Evolution of the ablated fiber morphology as a function of the dimensionless parameters A, and Sh.

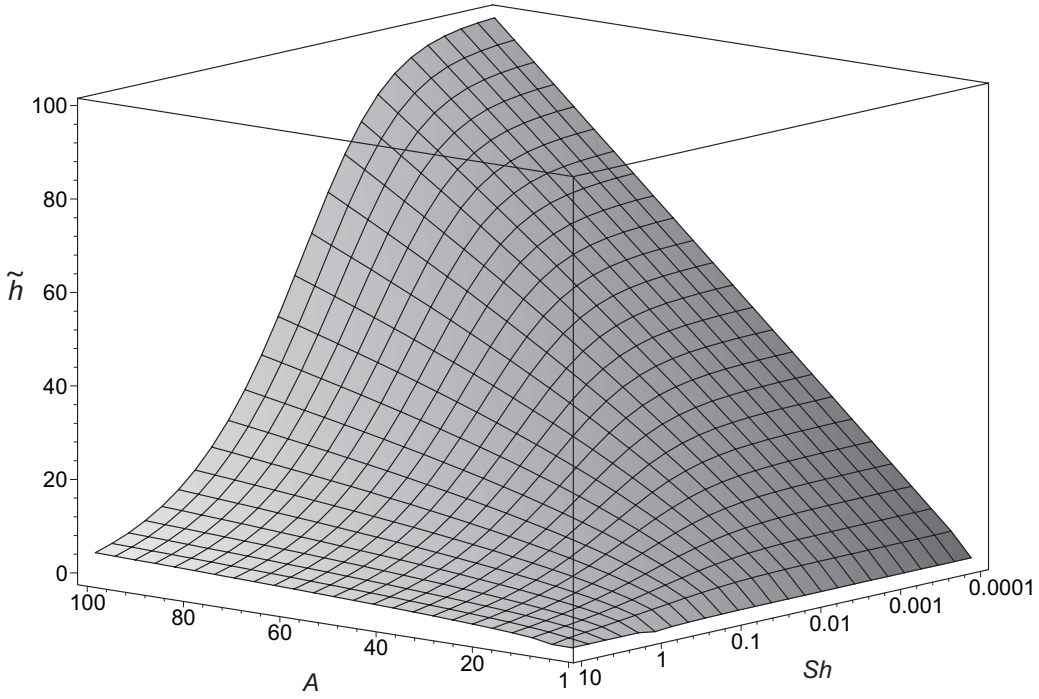

Fig. 6. Plot of the reduced height $\widetilde{h}$ as a function of A and Sh.

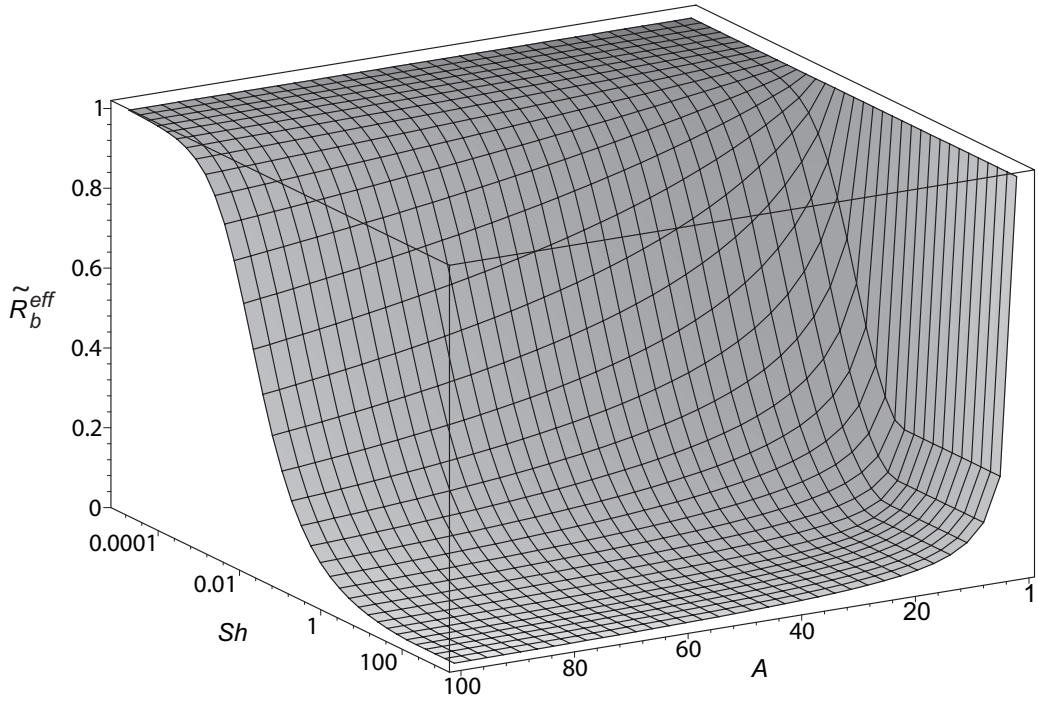

Fig. 7. Normalized effective ablation velocity of a bundle $\widetilde{R}_b^{eff}$ as a function of A and Sh.

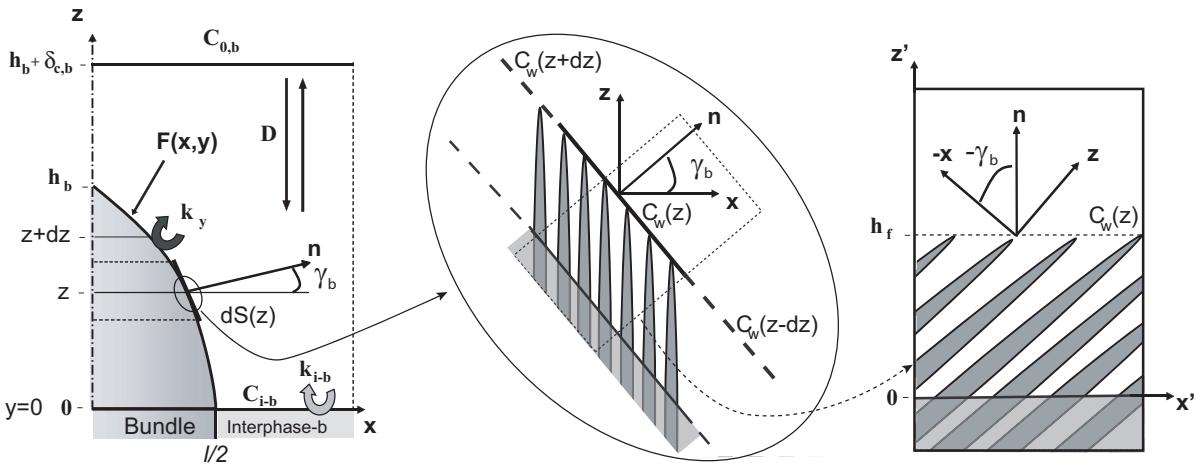

Fig. 8. Scheme of the multi-scale surface roughness and of the associated multi-scale model for a C/C composite.

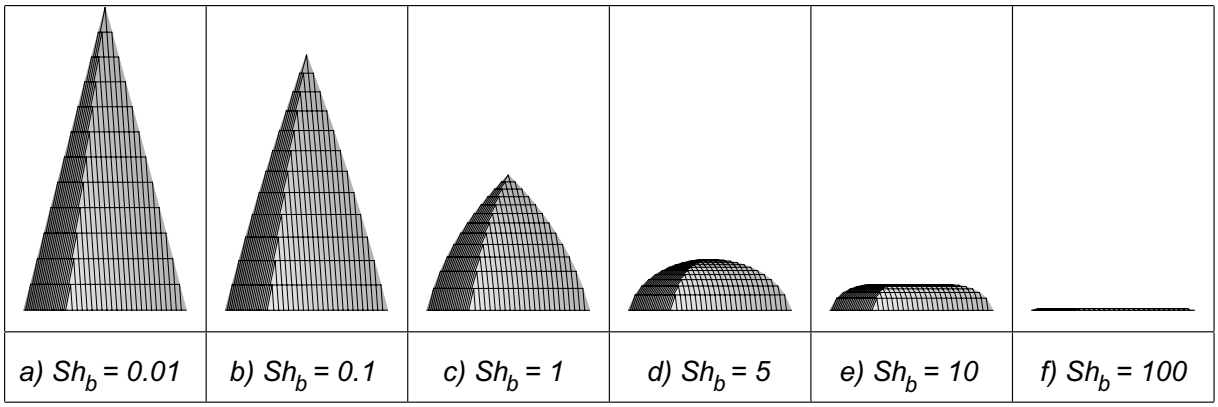

Fig. 9. Square-sectioned bundle morphology at steady state as a function of Sh_b (with $A_b = 5$).

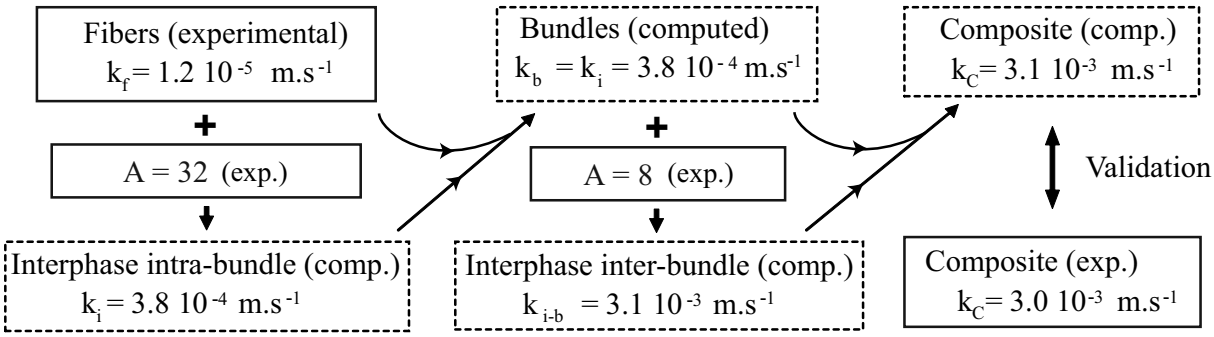

Fig. 10. Scheme of the multi-scale validation (3D C/C composite, dry air, atm. pressure, 898 K).